Hydrothermal Synthesis, Structural Characteristics, and Enhanced Photocatalysis of SnO$_2$/α-Fe$_2$O$_3$ Semiconductor Nanoheterostructures

Mutong Niu, Feng Huang, Lifeng Cui, Ping Huang, Yunlong Yu, and Yuansheng Wang*

State Key Laboratory of Structural Chemistry, Fujian Institute of Research on the Structure of Matter, Chinese Academy of Sciences, Graduate University of Chinese Academy of Sciences, Fuzhou, Fujian 350002, China

Nanoheterostructure, which consists of chemically distinct components, has demonstrated great potential for revolutionizing nanomaterial research by providing a means to define diverse functionalities within a single nanostructure and, moreover, to generate novel properties nonexistent in the individual component materials arising from the strong interfacial interactions at the nanoscale.[1−3] In recent years, tremendous efforts have been devoted to the fabrication of SNHs by various vapor-phase strategies.[3−5] Apart from costly equipment for high vacuum and heating temperature, the previously reported vapor-phase methods generally lack flexibility in structural control on the products due to the instant reaction within an obturated system and can not be easily extended to construct SNHs of new configurations or compositions. As an economic alternative, fabricating SHNs in solution has the advantage of being low-cost, mild, and more controllable in the reaction process. With a "surfactant-controlled growth in a hot organic solvent" strategy, many metal chalcogenide SNHs with core/shell or multipod configurations have been successfully constructed.[1,6,7] Although some metal-oxide-based nanoheterostructures were synthesized *via* colloidal methods,[8] the reports on solution fabrication of SNHs, comprising pure metal oxides, are relatively rare.

α-Fe$_2$O$_3$ and SnO$_2$, two of the most studied semiconductors, have been intensively investigated as gas sensors,[9] electrodes,[10,11] and photocatalysts.[12,13] With a narrow band gap (~2.2 eV), α-Fe$_2$O$_3$ displays a wide photoelectrochemical response reaching the visible light region, but the holes in its valence band have relative low oxidation ability.[14] Although SnO$_2$ has a low valence band edge potential, which endows the holes in the band with high oxidation ability, it has no absorption to the light with a wavelength longer than 330 nm for its wide band gap (~3.8 eV).[15] A superior photocatalyst combining both merits of α-Fe$_2$O$_3$ and SnO$_2$ might be expected by constructing the SnO$_2$/α-Fe$_2$O$_3$ SNHs. Recently, the branched SnO$_2$/α-Fe$_2$O$_3$ SNHs[16] were prepared by introducing α-Fe$_2$O$_3$ nanotubes into a reverse microemulsion system, which was originally designed for fabricating pure SnO$_2$ nanorods.[17] However, this method involves poisonous organic solvents of great volume, which would not only complicate the experimental process but also passivate the surface reactivity of the products.

In this paper, we successfully prepared the branched SnO$_2$/α-Fe$_2$O$_3$ SNHs with high purity based on α-Fe$_2$O$_3$ nanospindles and nanocubes, respectively, in a hydrothermal system of Sn(OH)$_6$$^{2−}$ dilute

ABSTRACT Branched SnO$_2$/α-Fe$_2$O$_3$ semiconductor nanoheterostructures (SNHs) of high purity were synthesized by a low-cost and environmentally friendly hydrothermal strategy, through crystallographic-oriented epitaxial growth of the SnO$_2$ nanorods onto the α-Fe$_2$O$_3$ nanospindles and nanocubes, respectively. It was demonstrated that the SnO$_2$ nanorods would change their preferential growth direction on the varied α-Fe$_2$O$_3$ precursors with distinct crystallographic surface, driven by decrease in the distortion energy induced by lattice mismatch at the interfaces. All of the prepared SNHs were of high purity, ascribing to the successful preinhibition of the SnO$_2$ homonucleation in the reaction system. Significantly, some of the SnO$_2$/α-Fe$_2$O$_3$ SNHs exhibited excellent visible light or UV photocatalytic abilities, remarkably superior to their α-Fe$_2$O$_3$ precursors, mainly owing to the effective electron—hole separation at the SnO$_2$/α-Fe$_2$O$_3$ interfaces.

KEYWORDS: semiconductor · nanoheterostructure · epitaxial growth · hierarchical assembly · photocatalysis

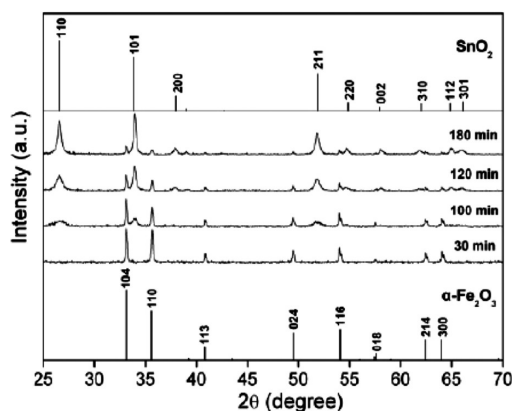**Figure 1.** XRD patterns of products at various reaction stages, with α-Fe₂O₃ nanospindles as precursors. The standard α-Fe₂O₃ and SnO₂ patterns are placed at the bottom and top, respectively.

aqueous solution. Noticeably, the homonucleation of SnO_2 was preinhibited in the reaction (*i.e.*, the SnO_2 phase was not generated when excluding the α-Fe_2O_3 precursors), which guaranteed the high purity of the SNHs. The structure features of the SnO_2/α-Fe_2O_3 SNHs at various reaction stages were investigated aiming to explore the formation mechanism of the SNHs and the influence of the distinct α-Fe_2O_3 precursors on the growth mode of SnO_2, which would provide us with deep insights into the elaborate structure architecting and functionality tailoring of the SNHs. The band configuration of the semiconductor is a critical factor affecting its property.[18] To reveal how the SNHs with reconstructed band gap structure affect the photocatalytic ability of the semiconductor, comparative investigations on the visible light or UV photocatalytic activities

of the bare α-Fe_2O_3 precursors and their SnO_2/α-Fe_2O_3 SNHs counterparts were performed.

RESULTS AND DISCUSSION

SnO_2/α-Fe_2O_3 (Nanospindle) SNHs. Powder X-ray diffraction (XRD) patterns of the products obtained at various reaction stages, with α-Fe_2O_3 nanospindles as the seeding precursors, are presented in Figure 1. For the sample having reacted for 30 min, there was only the hexagonal α-Fe_2O_3 phase (PDF 330664). When the reaction was prolonged to 100, 120, and finally 180 min, the tetragonal SnO_2 phase (PDF 770450) was formed and increased continuously in quantity. Figure 2 presents the scanning electron microscopy (SEM) images of the products at various reaction stages. The presynthesized α-Fe_2O_3 nanospindle precursors were generally of *ca.* 500 nm in length and *ca.* 150 nm in diameter (Figure 2a). Their length axis was determined to be along [001] of the hexagonal α-Fe_2O_3 by selected area electron diffraction in the transmission electron microscope (TEM). For the sample having reacted for 30 min, no visible changes were found. When the reaction proceeded to 100 min, many 5 nm sized SnO_2 particles precipitated on the surfaces of the α-Fe_2O_3 nanospindles, making the products appear as balsam pears (Figure 2b). As the reaction was prolonged to 120 min, the SnO_2 particles evolved to short nanorod arrays, and the product exhibited a corn-like morphology (Figure 2c). After reacting for 180 min, an interesting SnO_2/α-Fe_2O_3 branched nanostructure of 6-fold symmetry, with six solid SnO_2 strips longitudinally enwrapping the α-Fe_2O_3 nanospindle, resulted with high purity, as shown in Figure 2d. Further prolonging the reaction to 240 min led
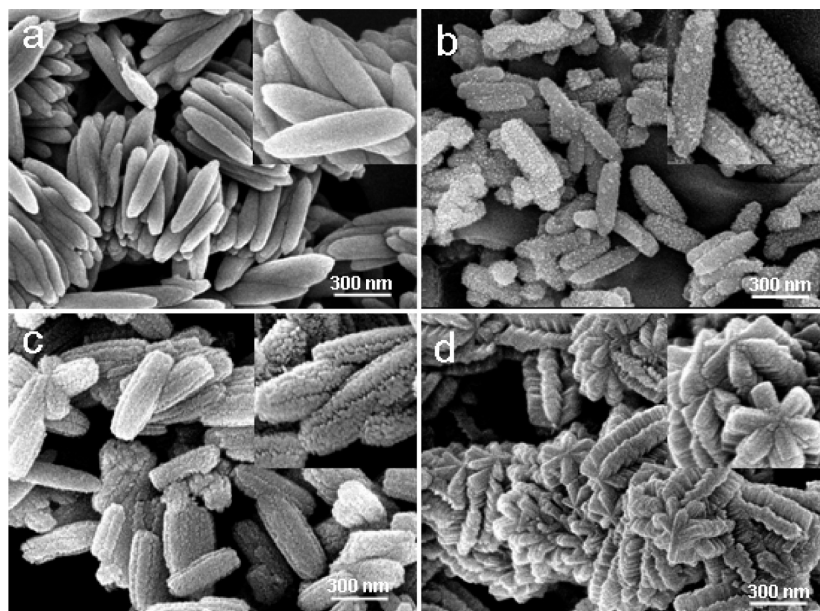

Figure 2. SEM micrographs of products at various reaction stages: (a) presynthesized α-Fe₂O₃ nanospindle precursors; (b) having reacted for 100 min; (c) having reacted for 120 min; (d) having reacted for 180 min. Insets show magnified images of the corresponding products.
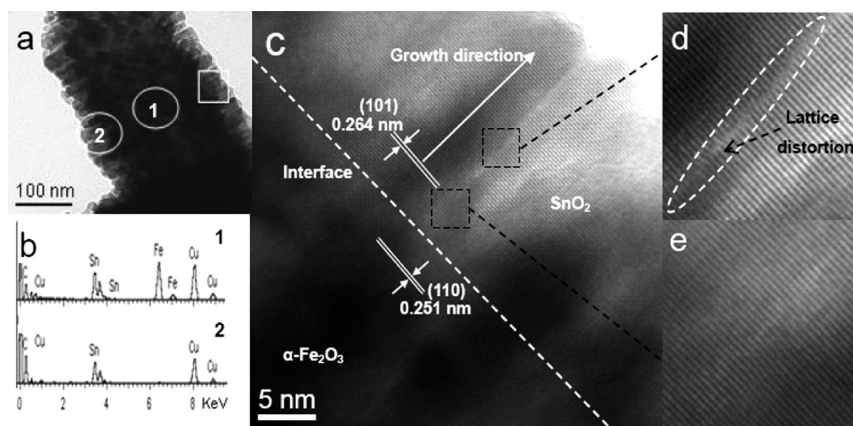
Figure 3. (a) TEM micrograph of a segment of corn-like SnO$_2$/α-Fe$_2$O$_3$ composite; (b) EDS spectra taken from encircled region 1 and 2, respectively, in (a), revealing composition change of composite, Cu signals were from copper grid supporting the specimen; (c) HRTEM image recorded from frame marked region in (a), showing crystallographic-oriented epitaxial growth of SnO$_2$ nanorods on the (110) plane of α-Fe$_2$O$_3$ nanospindle; (d,e) magnified images of the frame marked regions in (c), showing the merging of two adjacent SnO$_2$ nanorods.

to a volume expansion of the SnO$_2$ strips, as shown in Figure S2 in the Supporting Information.

To explore how the SnO$_2$ phase couples with the α-Fe$_2$O$_3$ nanospindle, TEM observations of the SnO$_2$/α-Fe$_2$O$_3$ branched nanostructure in the 120 min reacted sample were conducted, as presented in Figure 3. Figure 3a shows a segment of the corn-like SnO$_2$/α-Fe$_2$O$_3$ composite with diameter of *ca.* 200 nm. Evidently, its center part was enriched with Fe and Sn, while Fe vanished at the edge, as revealed by the energy-dispersive X-ray spectrometer (EDS) spectra in Figure 3b. The interfacial structure of the SnO$_2$/α-Fe$_2$O$_3$ composite was identified by high-resolution TEM (HRTEM) observation presented in Figure 3c. The (101) planes of SnO$_2$ stacked parallel to the (110) ones of α-Fe$_2$O$_3$. In other words, the SnO$_2$ nanorods epitaxially grew along the normal direction of (101)$_{SnO_2}$ on the (110) surface of the α-Fe$_2$O$_3$ precursor, forming a flat (101)$_{SnO_2}$/(110)$_{α-Fe_2O_3}$ interface (heterojunction). The preferential growth of the SnO$_2$ nanorods along the normal of (101) planes was also evidenced by the fact that the relative intensity of the (101)$_{SnO_2}$ XRD peak is much stronger than that in the standard XRD pattern of SnO$_2$. Figure 3d,e shows the magnified HRTEM images of the frame marked regions in panel b, which indicates that the adjacent SnO$_2$ nanorods incline to merge together to form a monocrystal in the course of growth. At the beginning of merging,

there were obvious lattice distortions in the connecting region (Figure 3d). However, with further growth of the nanorods, these lattice distortions were released completely, forming a coalescence between the adjacent nanorods (Figure 3e). As the result of the lateral emerging growth of the SnO$_2$ nanorods, the solid SnO$_2$ monocrystalline strips along the length axis of the α-Fe$_2$O$_3$ nanospindle were formed in the sample having reacted for 180 min (Figure S1 in the Supporting Information). The growth of the SnO$_2$ strips on the six (110)$_{α-Fe_2O_3}$ planes surrounding the [001] axis of the hexagonal α-Fe$_2$O$_3$ nanospindle resulted in the final 6-fold symmetrically branched SnO$_2$/α-Fe$_2$O$_3$ SNHs.

On the basis of the results stated above, the formation process of the hierarchically assembled SnO$_2$/α-Fe$_2$O$_3$ SNHs from the α-Fe$_2$O$_3$ nanospindle precursors in hydrothermal system is concluded, as illustrated schematically in Figure 4. First, the SnO$_2$ nanoparticles heteronucleate through dehydration of Sn(OH)$_6^{2-}$ and then epitaxially grow on the surfaces of the α-Fe$_2$O$_3$ precursors, forming the (101)$_{SnO_2}$/(110)$_{α-Fe_2O_3}$ interfaces. Second, these particles grow up into aligned nanorod arrays on the 6-fold symmetrical (110) planes of the α-Fe$_2$O$_3$ nanospindles, taking the normal of (101) planes as the preferential growth direction. As the reaction further proceeds, the adjacent SnO$_2$ nanorods tend to merge together to form the monocrystalline strip, re-
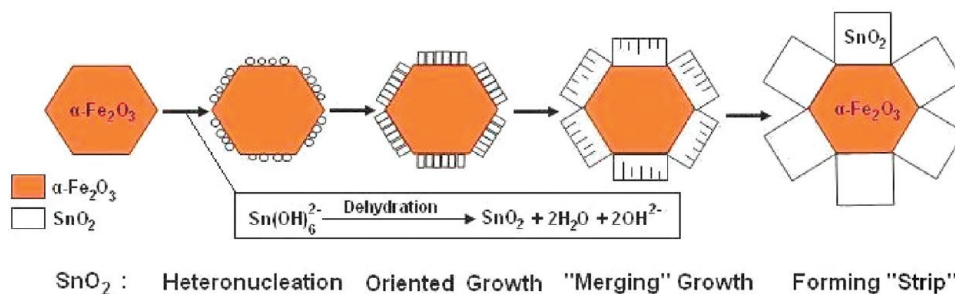

Figure 4. Schematically illustrated formation process of hierarchically assembled SnO$_2$/α-Fe$_2$O$_3$ SNHs based on α-Fe$_2$O$_3$ nanospindle precursor. The products at various reaction stages are represented by their idealized cross-section geometry.
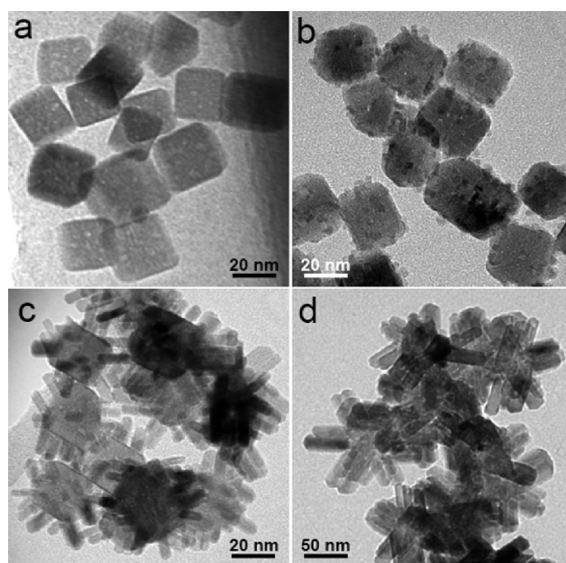
Figure 5. TEM micrographs of $SnO_2/\alpha\text{-}Fe_2O_3$ (nanocube) SNHs at various reaction stages: (a) presynthesized $\alpha\text{-}Fe_2O_3$ nanocube precursors; (b) having reacted for 90 min; (c) having reacted for 120 min; (d) having reacted for 180 min.

sulting finally in the 6-fold symmetrically branched $SnO_2/\alpha\text{-}Fe_2O_3$ SNHs.

$SnO_2/\alpha\text{-}Fe_2O_3$ (Nanocube) SNHs. To explore how the varied $\alpha\text{-}Fe_2O_3$ precursors affect the heteronucleation and growth of SnO_2 phase, the $\alpha\text{-}Fe_2O_3$ nanocubes (Figure S3 in the Supporting Information), which might provide distinct exposure surfaces to form the interfaces with SnO_2, were employed as the reaction precursors. The XRD pattern and SEM image of the $SnO_2/\alpha\text{-}Fe_2O_3$ SNHs having hydrothermally reacted for 180 min are presented in Figures S4 and S5, respectively. The $SnO_2/\alpha\text{-}Fe_2O_3$ SNHs were of high purity, and $\alpha\text{-}Fe_2O_3$ nanocubes were completely enwrapped by the SnO_2 nanorods. The formation process of the hierarchically assembled $SnO_2/\alpha\text{-}Fe_2O_3$ (nanocube) SNHs was revealed by TEM observations of the products at various reaction stages shown in Figure 5. Basically, the SnO_2 nanorods were generated on the surfaces of the $\alpha\text{-}Fe_2O_3$ nanocubes through heteronucleation, crystallographic-oriented growth, and merging stages, similar to the case discussed above for the $SnO_2/\alpha\text{-}Fe_2O_3$ (nanospindle) SNHs. Noticeably, as exhibited by HRTEM images shown in

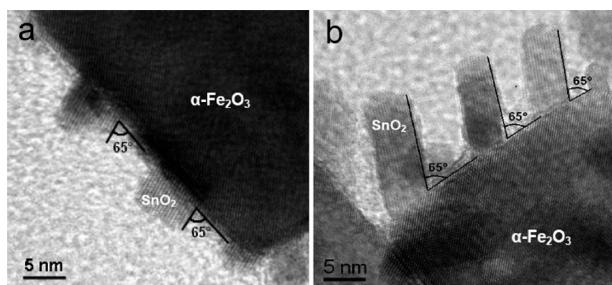**Figure 6.** HRTEM micrographs of $SnO_2/\alpha\text{-}Fe_2O_3$ (nanocube) SNHs at different reaction stages: (a) having reacted for 90 min; (b) having reacted for 120 min, showing slanted growth of SnO_2 nanorods on surfaces of $\alpha\text{-}Fe_2O_3$ nanocubes with a fixed angle of *ca.* 65°.

Figure 6, all the SnO_2 nanorods grew slantwise on the surfaces of the $\alpha\text{-}Fe_2O_3$ nanocubes with a fixed angle of *ca.* 65° during the reaction.

It has been demonstrated in our previous paper[19] that the $\alpha\text{-}Fe_2O_3$ nanocube was enclosed by six identical planes indexed as (101) in the trigonal system (herein, in order to simplify the analysis, their indexes are transformed to (012) in the hexagonal system). As exhibited by the HRTEM image of the interfacial region in a $SnO_2/\alpha\text{-}Fe_2O_3$ (nanocube) SNH shown in Figure 7, and the fast Fourier transform (FFT) patterns taken from $\alpha\text{-}Fe_2O_3$ and SnO_2 (the top and bottom insets, respectively, in Figure 7), the SnO_2 nanorod provided the (101) plane to form the interface with the (012) plane of the $\alpha\text{-}Fe_2O_3$ precursor and grew preferentially along the normal of its (112) plane. Herein, a question arises: why did the SnO_2 nanorods grew slantwise, instead of perpendicularly as the case for the $SnO_2/\alpha\text{-}Fe_2O_3$ (nanospindle) SNHs, on the surfaces of the $\alpha\text{-}Fe_2O_3$ nanocubes? To answer this question, the connection between $(110)_{\alpha\text{-}Fe_2O_3}$ and $(110)_{SnO_2}$ lattices at the interface of the $SnO_2/\alpha\text{-}Fe_2O_3$ (nanocube) SNH is illustrated schematically in the middle inset of Figure 7. The angle between $(110)_{\alpha\text{-}Fe_2O_3}$ and the interface ($(012)_{\alpha\text{-}Fe_2O_3}$) is 43°, while the angle between $(110)_{SnO_2}$ and the interface ($(101)_{SnO_2}$) is 66.7°. When the SnO_2 nanorod grows perpendicularly to the surface of the $\alpha\text{-}Fe_2O_3$ nanocube, the interfacial lattice mismatch between $(110)_{\alpha\text{-}Fe_2O_3}$ and $(110)_{SnO_2}$ reaches as large as 9.0% ($(0.365-0.335)/0.335 \times 100\% \approx 9.0\%$). However, when it grows slantwise, the interfacial lattice mismatch is dramatically reduced to 1.1% ($(0.369-0.365)/0.365 \times 100\% \approx 1.1\%$). The least lattice mismatch at the interface causes the least lattice distortion energy and results in the lowered heteronucleation energy barrier,[16,20,21] which determines the growth mode of the SnO_2 nanorods. Significantly, the connection between $(110)_{SnO_2}$ and $(110)_{\alpha\text{-}Fe_2O_3}$ lattices leads to a less-defective and abrupt interface, as revealed in Figure 7, which is beneficial to the transfer of the charge carriers.[3,22,23] Similar reasoning on the epitaxial relationship of the TiO_2/Co nanoheterostructures has been reported by Casavola *et al.*[24]

Photocatalysis of $SnO_2/\alpha\text{-}Fe_2O_3$ SNHs. The MB degradabilities of the $\alpha\text{-}Fe_2O_3$ nanospindle precursors and their $SnO_2/\alpha\text{-}Fe_2O_3$ SNHs counterparts under visible light irradiation for 4 h are presented in Figure 8a. Herein, FS represents $\alpha\text{-}Fe_2O_3$ nanospindle precursors, while FSS-100, FSS-120, FSS-180, and FSS-240 represent $SnO_2/\alpha\text{-}Fe_2O_3$ (nanospindle) SNHs having reacted for 100, 120, 180, and 240 min, respectively. Although the photocatalytic abilities of the $SnO_2/\alpha\text{-}Fe_2O_3$ SNHs varied with their fabrication time, they were all superior to that of the $\alpha\text{-}Fe_2O_3$ precursors. With increase in fabrication time, the photocatalysis of the $SnO_2/\alpha\text{-}Fe_2O_3$ SNHs increased, reaching a maximum for the sample having reacted for 180 min, and it decreased when the reaction was further prolonged. Similar results were also ob-

tained for the SnO_2/α-Fe_2O_3 (nanocube) SNHs, with the sample having reacted for 120 min (denoted as FCS-120) displaying the optimized photocatalytic performance, as exhibited in Figure S7. As a comparison, the MB degradabilities of the SnO_2/α-Fe_2O_3 SNHs with different α-Fe_2O_3 precursors and the N-doped TiO_2 powder (denoted as NT-500) which was reported having high visible light photocatalytic ability,[25] are presented in Figure 8b. Noticeably, both SNHs samples (FSS-180 and FCS-120) exhibited excellent visible light photocatalytic performances approaching to that of NT-500.

As we have known, SnO_2 has no absorption response to the visible light due to its wide band gap; therefore, the light absorption of SnO_2/α-Fe_2O_3 SNHs was solely contributed by the α-Fe_2O_3 component in the visible light photocatalysis experiments. The SNH samples contain less α-Fe_2O_3 than the pure α-Fe_2O_3 one with same weight. For example, α-Fe_2O_3 was about 32 wt % in the FSS-180 sample estimated by the XRD quantitative analysis. However, all of the SNH samples exhibited better enhanced visible light photocatalytic efficiency than the pure α-Fe_2O_3 ones, which must be correlated to the complexed band configuration of the SnO_2/α-Fe_2O_3 SNHs. On the basis of the Anderson model,[26] a "staggered" type II band configuration at the interface of the SnO_2/α-Fe_2O_3 SNHs is proposed, as shown in Figure 9. Under visible light irradiation, electrons (e$^-$) in the valence band (VB) of α-Fe_2O_3 were excited to its conduction band (CB), with same amount of holes (h$^+$) left in VB. Driven by the decreased potential energy, the photogenerated electrons in CB of α-Fe_2O_3 tended to transfer to that of SnO_2. Consequently, the photogenerated electrons and holes were separated at the SnO_2/α-Fe_2O_3 interfaces, which reduced their recombination probability and enabled them to migrate effectively to the surfaces of SnO_2 and α-Fe_2O_3, respectively, to form the hydroxyl radicals ($\bullet$OH). Although the oxygen radicals ($\bullet O_2^-$) would be formed first by the combination of electrons with O_2 adsorbed on the surfaces of SnO_2, they might transform to the hydroxyl radicals.[27] As a powerful oxidant, the hydroxyl radicals
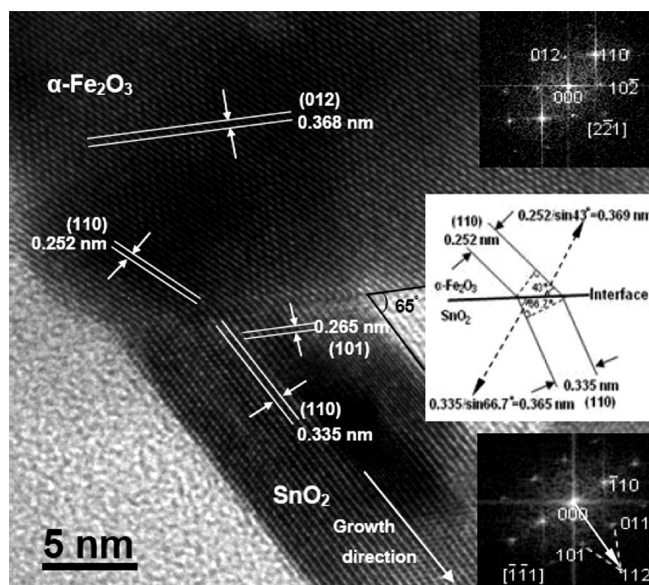

Figure 7. HRTEM micrograph of interfacial region in a SnO_2/α-Fe_2O_3 (nanocube) SNH, revealing crystallographic-oriented epitaxial growth of SnO_2 nanorod on α-Fe_2O_3 nanocube. Top and bottom insets are FFT patterns taken from α-Fe_2O_3 and SnO_2, respectively; middle inset illustrates schematically the connection between $(110)_{\alpha\text{-}Fe_2O_3}$ and $(110)_{SnO_2}$ lattices at the interface.

could decompose effectively the organic substances such as MB.[28]

The photocatalytic activity variation of the SnO_2/α-Fe_2O_3 SNHs having reacted for different durations can be explained as follows: at the early reaction stages, the heteronucleated SnO_2 nanoparticles scattered on the surfaces of the α-Fe_2O_3 precursors, and the SnO_2/α-Fe_2O_3 interfacial area increased with the reaction time, bringing in more interfacial charge separation and therefore enhanced photocatalytic activity of the SNHs sample. On the basis of the SEM images shown in Figure 2, the areas of the α-Fe_2O_3 surface covered by SnO_2 seem nearly same for the 120 min and the 180 min reacted samples, the obvious enhancement in the catalytic performance of the latter is probably due to its better crystallinity and less crystalline defects, such as dislocations and lattice distortions that might act as

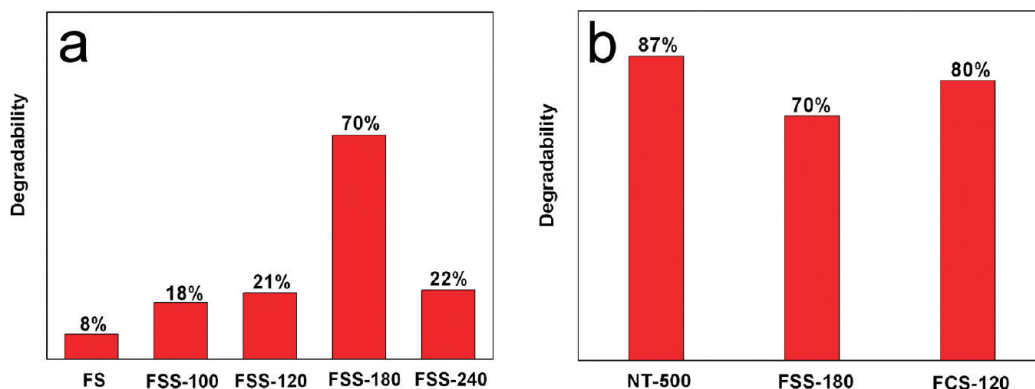Figure 8. (a) MB degradabilities of α-Fe_2O_3 nanospindle precursors and their SnO_2/α-Fe_2O_3 SNHs counterparts, and (b) MB degradability comparison among SnO_2/α-Fe_2O_3 SNHs and N-doped TiO_2 photocatalysts, under visible light irradiation for 4 h.
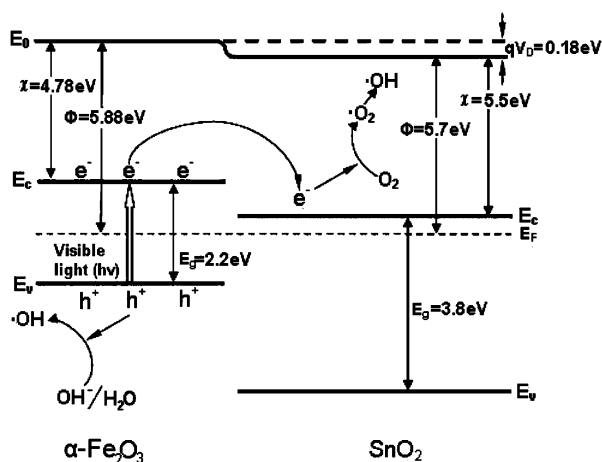
Figure 9. Schematic diagram showing band configuration and electron−hole separation at interface of $SnO_2/\alpha\text{-}Fe_2O_3$ SNHs under visible light irradiation; χ is the electron affinity, Φ the work function, V_D the contact potential, E_0 the vacuum level, E_c the bottom of conduction band, E_v the top of valence band, E_g the band gap, of $\alpha\text{-}Fe_2O_3$ or SnO_2 semiconductor.[29−31] E_F denotes Fermi level of $SnO_2/\alpha\text{-}Fe_2O_3$ SNHs.

Figure 10. MB degradabilities comparison among $\alpha\text{-}Fe_2O_3$ precursors, $SnO_2/\alpha\text{-}Fe_2O_3$ SNHs, and P25 photocatalyst, under UV irradiation for 40 min.

the recombination centers for the charge carriers in the SnO_2 crystals. The decrease of the catalysis for the 240 min reacted sample can be mainly attributed to the decrease of the $\alpha\text{-}Fe_2O_3$ content in the SNHs which weakened the visible light absorption. In addition, another factor depressing the catalysis might be the obvious dimension expansion of the SnO_2 strips which prolonged the migration distance of the interface-separated electrons to the surfaces of SnO_2 and increased their recombination risk.

The MB degradabilities of the $\alpha\text{-}Fe_2O_3$ precursors and their $SnO_2/\alpha\text{-}Fe_2O_3$ SNHs counterparts under UV irradiation for 40 min are presented in Figure 10. Herein, FC represents $\alpha\text{-}Fe_2O_3$ nanocube precursors, and P25 is the commercial UV photocatalyst produced by Degussa Company. The photocatalytic abilities of both FSS-180 and FCS-120 were remarkably enhanced compared with their $\alpha\text{-}Fe_2O_3$ precursors. Significantly, FSS-180 degraded 84% MB, approaching that of P25 (97%). The factors inducing the excellent UV catalysis of the SNHs are complicated. However, the electron−hole separation at the $SnO_2/\alpha\text{-}Fe_2O_3$ interfaces must be a critical one. Unlike the case in the visible light photocatalysis,
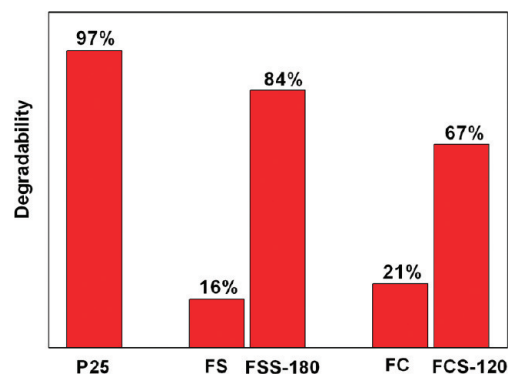
both $\alpha\text{-}Fe_2O_3$ and SnO_2 here have the adsorption response to the UV irradiation. Consequently, the interfacial electron−hole separation in SNHs would be bidirectional; that is, the photogenerated electrons on CB of $\alpha\text{-}Fe_2O_3$ inclined to transfer to CB of SnO_2 with lower potential, while the holes on VB of SnO_2 transfer to VB of $\alpha\text{-}Fe_2O_3$ with higher potential, as illustrated in Figure S10 in the Supporting Information.

CONCLUSIONS

In summary, a hydrothermal strategy was developed to synthesize branched $SnO_2/\alpha\text{-}Fe_2O_3$ SNHs through hierarchical assembly, that is, crystallographic-oriented epitaxial growth of SnO_2 nanorods onto $\alpha\text{-}Fe_2O_3$ nanospindles or nanocubes. The investigation on the structure evolution of the $SnO_2/\alpha\text{-}Fe_2O_3$ SNHs indicated a "three-stage" formation mechanism for the mature SNHs, that is, heteronucleation, crystallographic-oriented growth, and finally merging growth of the SnO_2 nanorods on $\alpha\text{-}Fe_2O_3$ precursors. The lattice mismatch at the interface played an important role in determining the growth of SnO_2 and resulted in the varied preferential growth direction of the SnO_2 nanorods on the $\alpha\text{-}Fe_2O_3$ precursors with distinct crystallographic surfaces. Evidently, the formation of $SnO_2/\alpha\text{-}Fe_2O_3$ SNHs remarkably enhanced the visible light or UV photocatalytic ability of the nanocrystalline $\alpha\text{-}Fe_2O_3$, mainly owing to the effective electron−hole separation at the interfaces of the SNHs.

EXPERIMENTAL SECTION

Sample Synthesis: The $\alpha\text{-}Fe_2O_3$ precursors of nanospindles[32] and nanocubes[19] were presynthesized based on the previously reported hydrothermal or solvothermal methods. The $SnO_2/\alpha\text{-}Fe_2O_3$ SNHs were prepared by a surfactant-free hydrothermal strategy. Typically, 0.010 g of the definite $\alpha\text{-}Fe_2O_3$ precursors was dispersed in the $Sn(OH)_6^{2-}$ dilute aqueous solution premade by dissolving 0.087 g of $SnCl_4 \cdot 5H_2O$ and 0.267 g of NaOH into 15 mL of deionized water. After ultrasonication for 10 min, the mixture was transferred into a 25 mL Teflon-lined stainless autoclave and heated at 220 °C for various durations. The resulting products were collected by centrifugation, washed with deion-

ized water and absolute ethanol for several times, and finally dried at 50 °C for 4 h in a vacuum. All of the reagents are of analytical grade and used as received.

Sample Characterization: Phase structures of the synthesized samples were characterized by X-ray diffraction (XRD) on a PANalytical X'Pert PRO diffractometer using Cu Kα (λ = 0.154 nm) radiation at a scanning rate of 5°/min for 2θ ranging from 5 to 85°. The microstructure and composition analyses were conducted on a JSM-6700F field emission scanning electron microscope (SEM) working at 5 kV and a JEM-2010 transmission electron microscope (TEM) equipped with an energy-dispersive X-ray spectrometer (EDS) working at 200 kV. The visible light diffuse reflectance spectra of the $\alpha\text{-}Fe_2O_3$ nanospindles and SnO_2/α-

Fe$_2$O$_3$ (nanospindles) SNHs were recorded using a Perkin-Elmer UV WinLab Lambda 900 UV/vis spectrophotometer, with BaSO$_4$ as the reference.

Photocatalysis Test: A heteropolyaromatic dye of methylene blue (MB) was adopted as the probe molecule to evaluate the photocatalytic activity of the samples under visible light or UV irradiation at room temperature. The visible light photocatalysis test was conducted in a 90 mL glass bottle. A 300 W tungsten halogen lamp positioned about 5 cm away from one side of the bottle, with a cutoff filter to remove the radiations below 420 nm and beyond 800 nm, was used as the illuminating source. Typically, 50 mg of samples was dispersed in 80 mL of 1×10^{-5} M MB aqueous solution to form the testing suspension. The UV photocatalysis test was performed in a 200 mL quartz tube. Four 4 W UV lamps (Philips, TUV 4W/G4 T5) with wavelength centered at 254 nm were used as illuminating source. Typically, 50 mg of samples was suspended in 150 mL of 1×10^{-5} M MB aqueous solution to form the testing suspension. All of the suspensions were magnetically stirred in dark for 12 h to ensure the establishment of absorption/desorption equilibrium of MB on the sample surfaces before the irradiation. During the irradiation, 4 mL aliquots were sampled at the given time intervals and centrifuged to remove the catalysts and were then analyzed on a Perkin-Elmer UV WinLab Lambda 35 spectrophotometer. The degradability of MB is represented by C/C_0, where C_0 and C denote the main absorption peak intensities of MB at 660 nm before and after irradiation.

Supporting Information Available: TEM and SEM micrographs, photocatalysis testing results and a proposed scheme illustrating the electron−hole separation mechanism under UV irradiation of the SNHs. This material is available free of charge *via* the Internet at http://pubs.acs.org.

REFERENCES AND NOTES

1. Milliron, D. J.; Hughes, S. M.; Cui, Y.; Manna, L.; Li, J. B.; Wang, L. W.; Alivisatos, A. P. Colloidal Nanocrystal Heterostructures with Linear and Branched Topology. *Nature* **2004**, *430*, 190–194.

2. Ouyang, L.; Maher, K. N.; Yu, C. L.; McCarty, J.; Park, H. Catalyst-Assisted Solution Liquid Solid Synthesis of CdSe Nanorod Heterostructure. *J. Am. Chem. Soc.* **2007**, *129*, 133–138.

3. Mieszawska, A. J.; Jalilian, R.; Sumanasekera, G. U.; Zamborini, F. P. The Synthesis and Fabrication of One-Dimensional Nanoscale Heterojunctions. *Small* **2007**, *3*, 722–756.

4. Lao, J. Y.; Wen, J. G.; Ren, Z. F. Hierarchical ZnO Nanostructures. *Nano Lett.* **2002**, *2*, 1287–1291.

5. Wu, X.; Jiang, P.; Ding, Y.; Cai, W.; Xie, S. S.; Wang, Z. L. Mismatch Strain Induced Formation of ZnO/ZnS Heterostructured Rings. *Adv. Mater.* **2007**, *19*, 2319–2323.

6. Cozzoli, P. D.; Pellegrino, T.; Manna, L. Synthesis, Properties and Perspectives of Hybrid Nanocrystal Structures. *Chem. Soc. Rev.* **2006**, *35*, 1195–1208.

7. Yin, Y.; Alivisatos, A. P. Colloidal Nanocrystal Synthesis and the Organic−Inorganic Interface. *Nature* **2005**, *437*, 664–670.

8. Casavola, M.; Buonsanti, R.; Caputo, G.; Cozzoli, P. D. Colloidal Strategies for Preparing Oxide-Based Hybrid Nanocrystals. *Eur. J. Inorg. Chem.* **2007**, *2008*, 837–854.

9. Gopal, R. C. B.; Cao, W.; Tan, O. K.; Zhu, W. Preparation of Fe$_2$O$_3$(0.9)-SnO$_2$(0.1) by Hydrazine Method: Application as an Alcohol Sensor. *Sens. Acutators, B* **2002**, *81*, 170–175.

10. Hasobe, T.; Imahori, H.; Kamat, P. V.; Fukuzumi, S. Quaternary Self-Organization of Porphyrin and Fullerene Units by Clusterization with Gold Nanoparticles on SnO$_2$ Electrodes for Organic Solar Cells. *J. Am. Chem. Soc.* **2003**, *125*, 14962–14963.

11. Khan, S. U. M.; Akikusa, J. Photoelectrochemical Splitting of Water at Nanocrystalline α-Fe$_2$O$_3$ Thin-Film Electrodes. *J. Phys. Chem. B* **1999**, *103*, 7184–7189.

12. Yu, J.; Yu, X.; Huang, B.; Zhang, X.; Dai, Y. Hydrothermal Synthesis and Visible-Light Photocatalytic Activity of Novel Cage-like Ferric Oxide Hollow Spheres. *Cryst. Growth Des.* **2009**, *3*, 1474–1480.

13. Li, L.; Liu, J.; Su, Y.; Li, G.; Chen, X.; Qiu, X.; Yan, T. Surface Doping for Photocatalytic Purposes: Relations between Particle Size, Surface Modifications, and Photoactivity of SnO$_2$: Zn^{2+} Nanocrystals. *Nanotechnology* **2009**, *20*, 155706–155715.

14. Zhong, D. K.; Sun, J.; Inumaru, H.; Gamelin, D. R. Solar Water Oxidation by Composite Catalyst/α-Fe$_2$O$_3$ Photoanodes. *J. Am. Chem. Soc.* **2009**, *131*, 6086–6087.

15. Batzill, M.; Diebold, U. The Surface and Materials Science of Tin Oxide. *Pro. Surf. Sci.* **2005**, *79*, 47–154.

16. Zhang, D. F.; Sun, L. D.; Jia, C. J.; Yan, Z. G.; You, L. P.; Yan, C. H. Hierarchical Assembly of SnO$_2$ Nanorod Arrays on α-Fe$_2$O$_3$ Nanotubes: A Case of Interfacial Lattice Compatibility. *J. Am. Chem. Soc.* **2005**, *127*, 13492–13493.

17. Zhang, D. F.; Sun, L. D.; Yin, J. L.; Yan, C. H. Low-Temperature Fabrication of Highly Crystalline SnO$_2$ Nanorods. *Adv. Mater.* **2003**, *15*, 1022–1025.

18. Linsebigler, A. L.; Lu, G. Q.; Yates, J. T. Photocatalysis on TiO$_2$ Surfaces: Principles, Mechanisms, and Selected Results. *Chem. Rev.* **1995**, *95*, 735–758.

19. Zheng, Y. H.; Cheng, Y.; Wang, Y.; Bao, F.; Zhou, L.; Wei, X.; Zhang, Y.; Zheng, Q. Quasicubic α-Fe$_2$O$_3$ Nanoparticles with Excellent Catalytic Performance. *J. Phys. Chem. B* **2006**, *110*, 3093–3097.

20. Ding, Y.; Gao, P. X.; Wang, Z. L. Catalyst-Nanostructure Interfacial Lattice Mismatch in Determining the Shape of VLS Grown Nanowires and Nanobelts: A Case of Sn/ZnO. *J. Am. Chem. Soc.* **2004**, *126*, 2066–2072.

21. Wang, X. D.; Song, J. H.; Li, P.; Ryou, J. H.; Dupuis, R. D.; Summers, C. J.; Wang, Z. L. Growth of Uniformly Aligned ZnO Nanowire Heterojunction Arrays on GaN, AlN, and Al$_{0.5}$Ga$_{0.5}$N Substrates. *J. Am. Chem. Soc.* **2005**, *127*, 7920–7923.

22. Tak, Y. J.; Ryu, Y. H.; Yong, K. Atomically Abrupt Heteronanojunction of ZnO Nanorods on SiC Nanowires Prepared by a Two-Step Process. *Nanotechnology* **2005**, *16*, 1712–1716.

23. Yin, L. W.; Li, M. S.; Bando, Y.; Golberg, D.; Yuan, X.; Sekiguchi, T. Tailoring the Optical Properties of Epitaxially Grown Biaxial ZnO/Ge,and Coaxial ZnO/Ge/ZnO and Ge/ZnO/Ge Heterostructures. *Adv. Funct. Mater.* **2007**, *17*, 270–276.

24. Casavola, M.; Grillo, V.; Carlino, E.; Giannini, C.; Gozzo, F.; Fernandez-Pinel, E.; Garcia, M. A.; Manna, L.; Cingolani, R.; Cozzoli, P. D. Topologically Contrdolled Growth of Magnetic-Metal Functionalized Semiconductour Oxide Nanorods. *Nano Lett.* **2007**, *7*, 1386–1395.

25. Chen, X.; Wang, X.; Hou, Y.; Huang, J.; Wu, L.; Fu, X. The Effect of Postnitridation Annealing on the Surface Property and Photocatalytic Performance of N-Doped TiO$_2$ under Visible Light Irradiation. *J. Catal.* **2008**, *255*, 59–67.

26. Anderson, R. L. Experiments on Ge−GaAs Heterojunctions. *Solid-State Electron.* **1962**, *5*, 341–351.

27. Gnaser, H.; Savina, R. M.; Calaway, F. W.; Tripa, E. C.; Veryovkin, V. I.; Pellin, J. M. Photocatalytic Degradation of Methylene Blue on Nanocrystalline TiO$_2$: Surface Mass Spectrometry of Reaction Intermediates. *Int. J. Mass Spectrom.* **2005**, *245*, 61–67.

28. Zheng, Y.; Zheng, L.; Zhan, Y.; Lin, X.; Zheng, Q.; Wei, K. Ag/ZnO Heterostructure Nanocrystals: Synthesis, Characterization, and Photocatalysis. *Inorg. Chem.* **2007**, *46*, 6980–6986.

29. Xu, Y.; Schoonen, M. A. A. The Absolute Energy Positions of Conduction and Valence Bands of Selected Semiconducting Minerals. *Am. Mineral.* **2000**, *85*, 543–556.

30. Thimsen, E; Biswas, S.; Lo, C. S.; Biswas, P. Predicting the Band Structure of Mixed Transition Metal Oxides: Theory and Experiment. *J. Phys. Chem. C* **2009**, *113*, 2014–2021.

31. Trani, F.; Causà, M.; Ninno, D.; Cantele, G.; Barone, V. Density Functional Study of Oxygen Vacancies at the SnO_2 Surface and Subsurface Sites. *Phy. Rev. B* **2008**, *77*, 245410–245418.

32. Jia, C. J.; Sun, L. D.; Yan, Z. G.; You, L. P.; Luo, F.; Han, X. D.; Pang, Y. C.; Zhang, Z.; Yan, C. H. Single-Crystalline Iron Oxide Nanotubes. *Angew. Chem., Int. Ed.* **2005**, *44*, 4328–4333.